Mathematical Biology

Modelling and simulations of multi-component lipid membranes and open membranes via diffuse interface approaches

Xiaoqiang Wang · Qiang Du

Abstract   Diffuse interface (phase field) models are developed for multi-component vesicle membranes with different lipid compositions and membranes with free boundary. These models are used to simulate the deformation of membranes under the elastic bending energy and the line tension energy with prescribed volume and surface area constraints. By comparing our numerical simulations with recent biological experiments, it is demonstrated that the diffuse interface models can effectively capture the rich phenomena associated with the multi-component vesicle transformation and thus offering great functionality in their simulation and modelling.

X. Wang
School of Computational Sciences, Florida State University,
Tallahassee, FL 32306, USA
e-mail: xwang@scs.fsu.edu

Q. Du (✉)
Department of Mathematics and Department of Materials Science and Engineering,
Pennsylvania State University, University Park, PA 16802, USA
e-mail: qdu@math.psu.edu

1 Introduction

Lipid vesicle membranes are ubiquitous in biological systems. Studies of vesicle self-assembly and shape transition, including bud formation [29,30,37] and vesicle fission [14] are important in the understanding of cell functions. In recent experimental studies, multi-component vesicles with different lipid molecule compositions (and thus phases) have been shown to display even more complex morphology involving rafts and micro-domains [3,33]. There is strong evidence suggesting that phase segregation and interaction contribute critically to the membrane signaling, trafficking and sorting processes [39].

The geometric and topological structures of multi-component vesicles have been theoretically modeled by minimizing an energy with contributions of the bending resistance, that is the elastic bending energy, and the line tension at the interface between different components or the phase boundary [2,4,25,28,31]. The elastic bending energy first studied by Canham, Evans and Helfrich [12,13,34] for a single-phase membrane is defined as

$$E = \int_{\Gamma} \left(a_1 + a_2 (H - c_0)^2 + a_3 G \right) ds, \tag{1}$$

where H is the mean curvature of the membrane surface Γ, c_0 the spontaneous curvature, G the Gaussian curvature, a_1 the surface tension, a_2 the bending rigidity and a_3 the Gaussian rigidity or saddle-splay modulus. In recent experimental studies, it has been found that the bending rigidity in the liquid-disordered phase differs from that in the liquid-ordered phase in two-component membranes [2,3]. This can be attributed to, among other things, that the two phases have different lipid compositions or different concentrations of cholesterol molecules which serve as spacers between lipids. Thus, in the generalized bending elasticity model for two-component membranes, the bending rigidity a_2 is assumed to take values k_1 and k_2, respectively, in two different components (phases) $\Gamma_1 \subset \Gamma$ and $\Gamma_2 \subset \Gamma$ (with $\Gamma = \Gamma_1 \cup \Gamma_2$ and $\gamma_0 = \Gamma_1 \cap \Gamma_2$ being the common boundary between the two phases). In general, other parameters used in the model may also vary in different phases, however, we mainly focus on the effect of the bending rigidity in this paper, though the methodology can be easily extended to more general cases.

With the two phases co-existing on the membrane, it is natural to introduce a line tension on γ_0 to take into account the interfacial energy between the individual components [3,27,37]. Together with the bending elastic energy, this leads to the following energy for a two-component membrane

$$E = E_1 + E_2 + E_l = E_1 + E_2 + \int_{\gamma_0} \delta \, dl, \tag{2}$$

where δ is the line tension constant [27] and E_1 and E_2 are the bending elastic energy for the individual components, which are assumed to take a simpler form $E_i = \int_{\Gamma_i} k_i (H - c_i)^2 ds$ for $i = 1, 2$ in our consideration here. Note that the line

energy can also include the contribution of the geodesic curvature on γ_0 [2]. For example, by the Gauss–Bonnet theorem, for vesicles of the given Euler number, the effect of different Gaussian rigidities in the different components can be incorporated via the Euler-Poincare characteristics and a more general form of the line energy. We will not cover such general cases here though a brief discussion is provided in the Appendix B on the treatment of the Gaussian and geodesic curvatures. We note also that the effects of osmotic pressure and lateral tension are to be incorporated via the enforcement of constraints on the total volume and the surface areas of individual phases.

The basic mathematical model studied here can then be described as the minimization of the total energy defined by (2) for a two-component membrane with a prescribed total volume, and prescribed surface areas of both components. In order to effectively model and simulate the experimental findings on the exotic morphology of the multi-component vesicles (mostly taken from [3]), we extend the recently developed diffuse interface/phase field approach for the single-component vesicles [21] to the multi-component case, which avoids the tracking of the vesicle membrane by viewing the surface and phase boundary as the zero level sets of phase field functions. The general phase field framework has been used successfully in many applications [1,6,8,11]. For membrane deformation, this approach has become increasing popular in the research community in recent years. So far, its applications have mostly been confined to the case of using a single phase field function [5,17,18,26,32], albeit it is known that co-dimension two objects can be described effectively by a pair of level-set or phase field functions [7,11,35,38]. With the introduction of a second phase field function (order parameter), we demonstrate that the new two-component phase field model is capable of capturing the rich complex morphological changes experimentally observed in the two-component vesicle membranes. Thus, it may be a useful tool for the modelling and simulation of 3D multi-component vesicles with very general geometric shapes. Moreover, our model can be easily adapted to the case of an open membrane or a membrane with a free boundary (see [36] for an experimental study and [9,40–42,44] for analysis and computation). This is based on the observation that an open membrane can be thought as a two-component vesicle with a *virtual* component having zero bending rigidity. Further generalization is possible for vesicles with three or more components.

The paper is organized as follows: in Sect. 2, we present the diffuse interface/phase field formulation of the total energy (2) and the penalty formulation for the constraints. In Sect. 3, we first discuss the discretization and implementation issues and provide some convergence tests to validate our method, then we assemble a number of interesting experiments to explore the two-component vesicle shape transformations due to the changes of different parameters. The numerical simulations are compared with experimental findings including the merging and splitting of different components. In Sect. 4, we present the phase field formulation for open membranes and some numerical simulation results. We then conclude with some remarks in Sect. 5. Some technical derivations are provided in the appendix with the first part on a brief discussion on the sharp interface limit and the second part on the incorporation of Gaussian curvature contribution.

2 A diffuse interface model

We start by introducing a pair of phase field functions (ϕ, η), defined on a physical (computational) domain Ω in the 3D space. The function $\phi = \phi(\mathbf{x})$ is used so that the level set $\{\mathbf{x} : \phi(\mathbf{x}) = 0\}$ determines the membrane Γ, while $\{\mathbf{x} : \phi(\mathbf{x}) > 0\}$ represents the interior of the membrane (denoted by Ω_i) and $\{\mathbf{x} : \phi(\mathbf{x}) < 0\}$ the exterior (denoted by Ω_e). In the phase field models of a single-component vesicle, this is the only phase field function used [20].

Next, we take another closed surface $\Gamma_\perp$ defined on the domain Ω and being perpendicular to Γ, such that it is the zero level set $\{\mathbf{x} : \eta(\mathbf{x}) = 0\}$ of a phase field function $\eta = \eta(x)$ in Ω with $\{\mathbf{x} : \eta(\mathbf{x}) > 0\}$ being the interior of $\Gamma_\perp$ and $\{\mathbf{x} : \phi(\mathbf{x}) < 0\}$ the exterior. We thus take the part of Γ in the interior of $\Gamma_\perp$ as the first component Γ_1 and the remain part of Γ (denoted by Γ_2) makes up the second component. Note that there may be many choices to select $\Gamma_\perp$, but we are mostly interested in the level set $\{\mathbf{x} : \eta(\mathbf{x}) = \phi(\mathbf{x}) = 0\}$ which gives the boundary between the two components of the vesicle, with $\{\mathbf{x} : \eta(\mathbf{x}) > 0$ and $\phi(\mathbf{x}) = 0\}$ representing one component of the membrane while $\{\mathbf{x} : \eta(\mathbf{x}) < 0$ and $\phi(\mathbf{x}) = 0\}$ the other component.

In the phase field model, the functions η and ϕ are forced to be nearly constant-valued except in thin transition layers near the surfaces Γ and $\Gamma_\perp$, respectively. We use two small positive constant parameters ϵ and ξ to characterize the widths of the thin layers (also called the diffuse interfaces). We note that a phase field function (order parameter), like η, has been introduced in [26,32] to describe the phase segregation on the membranes. But, different from our phase field description of the surface Γ, an explicit construction of the membrane surface and a direct computation of the bending elastic energy are used there instead of the phase field representation of the membrane surface.

Similar to [17], we have the phase field elastic bending energy defined by

$$E(\phi, \eta) = \int_\Omega \frac{k(\eta)}{2\epsilon} \left(\epsilon \Delta\phi + \left(\frac{1}{\epsilon}\phi + c_0(\eta)\sqrt{2} \right)(1 - \phi^2) \right)^2 dx, \qquad (3)$$

where Δ denotes the Laplace operator and a variable bending rigidity is given by $k(\eta) = k + c \tanh(\eta/\xi)$, so that $k_1 = k + c$ corresponds to the value of the bending rigidity of one component and $k_2 = k - c$ the other. Similarly, $2c_0(\eta) = (c_1 + c_2) + (c_1 - c_2) \tanh(\eta/\xi)$, so that c_1 and c_2 correspond to the spontaneous curvatures in the two components, respectively. A few other functionals needed in our model are as follows:

$$L(\phi, \eta) = \int_\Omega \delta \left[\frac{\xi}{2}|\nabla\eta|^2 + \frac{1}{4\xi}(\eta^2 - 1)^2 \right] \left[\frac{\epsilon}{2}|\nabla\phi|^2 + \frac{1}{4\epsilon}(\phi^2 - 1)^2 \right] dx, \quad (4)$$

$$A(\phi) = \int_\Omega \left[\frac{\epsilon}{2}|\nabla\phi|^2 + \frac{1}{4\epsilon}(\phi^2 - 1)^2 \right] dx, \qquad (5)$$

$$V(\phi) = \int_\Omega \phi \, dx, \tag{6}$$

$$D(\phi, \eta) = \int_\Omega \tanh\left(\frac{\eta}{\xi}\right) \left[\frac{\epsilon}{2}|\nabla\phi|^2 + \frac{1}{4\epsilon}(\phi^2 - 1)^2\right] dx, \tag{7}$$

where ∇ denotes the gradient operator.

To reveal the meanings of above functionals, we follow similar discussions in [17] to assume an ansatz of the form $\phi(\mathbf{x}) \sim \tanh(d(\mathbf{x}, \Gamma)/(\sqrt{2}\epsilon))$ and $\eta(\mathbf{x}) \sim \tanh(d(\mathbf{x}, \Gamma_\perp)/(\sqrt{2}\xi))$ for the phase field functions. Here d denotes the signed distance function. In this ansatz, we can check that as ϵ and ξ tend to 0, that is, in the sharp interface limit,

$$E(\phi, \eta) \to \frac{4\sqrt{2}}{3} \sum_{j=1}^{2} \int_{\Gamma_j} k_j (H - c_j)^2 \, ds. \tag{8}$$

More details are given in the Appendix A, along with a brief derivation of the following asymptotic limits

$$V(\phi) \to |\Omega_i| - |\Omega_e|, \quad A(\phi) \to \frac{2\sqrt{2}}{3}|\Gamma|, \tag{9}$$

and

$$L(\phi, \eta) \to \frac{8}{9} \int_{\gamma_0} \delta \, dl, \quad D(\phi, \eta) \to \frac{2\sqrt{2}}{3}(|\Gamma_1| - |\Gamma_2|), \tag{10}$$

where $|\cdot|$ denotes either the enclosed volume of a 3D domain, or the area of a surface.

To re-cap the discussion, the total energy in the two-component phase field model is

$$\mathcal{E}(\phi, \eta) = E(\phi, \eta) + L(\phi, \eta), \tag{11}$$

while the constraints are given by

$$V(\phi) = v_d, \quad A(\phi) = a_0, \quad D(\phi, \eta) = a_d, \tag{12}$$

with v_d, a_0 and a_d being the prescribed volume difference (hence the interior volume is prescribed), the total surface area and the area difference between the two components (hence areas of both components are prescribed).

To maintain the consistency with the sharp interface model (2) of the phase field formulation which is based on ϕ and η having the tanh profiles and the orthogonality between Γ and $\Gamma_\perp$, additional constraints are imposed. First of all, the orthogonality constraint on the normal directions of the two surfaces, written in our phase field formulations, can be enforced by $\nabla\phi \cdot \nabla\eta = 0$ on or near the phase boundary $\{\mathbf{x} : \phi(\mathbf{x}) = \eta(\mathbf{x}) = 0\}$. With ϕ and η having tanh profiles, their gradients become small away from their zero level sets, the orthogonality constraint may thus be enforced

everywhere by penalizing

$$N(\phi, \eta) = \int_{\Omega} \frac{\epsilon}{2} |\nabla \phi \cdot \nabla \eta|^2 \, dx. \tag{13}$$

Second, to better maintain the tanh profile of η, especially for the case of a large line tension energy, we have two options, one is to add a small regularization term, much like the bending elastic energy for ϕ but with a very small bending rigidity; another option is to regularize through the following functional

$$P(\eta) = \int_{\Omega} \left(\frac{\xi}{2} |\nabla \eta|^2 - \frac{1}{4\xi} (\eta^2 - 1)^2 \right)^2 \, dx, \tag{14}$$

which also vanishes for a tanh profile.

Summarizing the above discussion, the variational phase field model for two-component vesicles is to minimize the total energy $\mathcal{E}(\phi, \eta) = E(\phi, \eta) + L(\phi, \eta)$ with constraints $V(\phi) = v_d$, $A(\phi) = a_0$, $D(\phi, \eta) = a_d$, while requiring $N(\phi, \eta)$ and $P(\eta)$ being small. So, by adding both the penalty and regularization terms, the vesicle surface and the phase boundary in between the two components are then determined by a pair of phase functions (ϕ, η) which minimizes the functional

$$\mathcal{E}_M(\phi, \eta) = E(\phi, \eta) + L(\phi, \eta) + \frac{1}{2} M_1 (V(\phi) - v_d)^2 + \frac{1}{2} M_2 (A(\phi) - a_0)^2$$
$$+ \frac{1}{2} M_3 (D(\phi, \eta) - a_d)^2 + \frac{1}{2} M_4 (N(\phi, \eta))^2 + \frac{1}{2} M_5 (P(\eta))^2 \tag{15}$$

where $\{M_i\}_{i=1}^3$ are penalty constants for the constraints on the volume and surface areas while $\{M_i\}_{i=4}^5$ are regularization constants for maintaining better control on the phase field functions.

3 Numerical simulations of two-component membranes

In this section, we compute the minima of the phase field energy (15) using various parameter values. For simplicity, we only consider the case where $c_1 = c_2 = 0$, this allows us to focus on examining how variations in the bending rigidities and the line tension parameter affect the vesicle shape deformation and the equilibrium configurations of two-component membranes. The more general cases involving the spontaneous curvatures and Gaussian curvatures are to be considered in the future.

Discretization and code development We take the 3D box $\Omega = [-\pi, \pi]^3$ as the spatial computational domain and assume that the membranes to be simulated can be well enclosed in the box. For simplicity, we choose to set $\xi = \epsilon$ in our numerical simulations. To solve (16) in Ω, with the computational box large enough and the

membrane being situated away from the box boundary, the phase field functions may be assumed to satisfy periodic boundary conditions.

To search for the energy minimizers, we adopt a gradient flow approach which has been very effective in solving the phase field model of single-component vesicles [20,22,43]. The equations for the gradient flow (defined with respect to a standard L^2 inner product) are given by

$$\phi_t = -\frac{\delta \mathcal{E}_M}{\delta \phi}, \quad \eta_t = -\frac{\delta \mathcal{E}_M}{\delta \eta} \tag{16}$$

where $\frac{\delta}{\delta \phi}$ and $\frac{\delta}{\delta \eta}$ denote the first variation with respect to the functions ϕ and η. Initial profiles, often taken to be similar to that are expected of the final equilibrium shape, are first prescribed. Then as time increases, the monotone decreasing of the energy $\mathcal{E}_M$ is ensured for $t > 0$, and asymptotically the gradient flow yields a minimizer of the energy. We note that the gradient flow often finds only stable local minima.

For the spatial discretization of (16), due to the use of periodic boundary condition and the regularization effect of the finite transition layer, for fixed ϵ, the spectral method is an efficient way to solve (16) with the use of adequate number of Fourier modes and the help of FFT routines [11,22].

A few options are implemented for the time discretization, such as an explicit forward Euler scheme:

$$\frac{\phi_{n+1} - \phi_n}{\Delta t_n} = -\frac{\delta \mathcal{E}_M}{\delta \phi}(\phi_n, \eta_n), \quad \frac{\eta_{n+1} - \eta_n}{\Delta t_n} = -\frac{\delta \mathcal{E}_M}{\delta \eta}(\phi_n, \eta_n),$$

where Δt_n is the time step size, or the backward Euler scheme

$$\frac{\phi_{n+1} - \phi_n}{\Delta t_n} = -\frac{\delta \mathcal{E}_M}{\delta \phi}(\phi_{n+1}, \eta_{n+1}), \quad \frac{\eta_{n+1} - \eta_n}{\Delta t_n} = -\frac{\delta \mathcal{E}_M}{\delta \eta}(\phi_{n+1}, \eta_{n+1}),$$

whose solution (ϕ_{n+1}, η_{n+1}) can be also cast as a minimizer of

$$\min \mathcal{E}_M(\phi, \eta) + \frac{1}{2\Delta t_n} \int_\Omega \left[|\phi - \phi_n|^2 + |\eta - \eta_n|^2 \right] d\Omega$$

which assures the monotone decreasing of the energy $\mathcal{E}_M$ for any time step Δt_n [23]. The convergence and stability properties of such schemes can be derived in similar ways as that in [23]. Another efficient alternative is a semi-implicit Euler scheme [20] which only lags nonlinear terms explicitly while treating the linear part implicitly. This is in fact an example of a class of operator splitting schemes. In all of these time stepping schemes, the time step Δt_n can change adaptively, and it is properly chosen to ensure the decay of energy, in particular for explicit and semi-implicit schemes. For efficient implementation of all the time stepping schemes with the Fourier spatial discretization, the differentiations in the space variables are implemented in the Fourier space via FFT while the nonlinear functions are evaluated in the real space at the Fourier nodes. Such a strategy eliminates the need of linear solvers for the update

of solution in time. We refer to [11] and [22] for more details. The simulation codes are implemented on both distributed memory systems via MPI and shared memory systems via OPENMP to improve their efficiency and functionality in conducting extensive 3D simulations. As we are aimed at performing full 3D simulations involving complex vesicle geometry, we do not utilize any special symmetry, thus possible incurring excessive CPU costs for special cases such as those of axis-symmetric shapes. A typical simulation takes about a day to complete on a Unisys ES7000 which has 16 Intel Itanium 2 processors. Recently, significant computational savings have been demonstrated for the adaptive finite element implementations of phase field simulations of single-component membranes, indicating that the mesh points need mostly to be concentrated near the membrane surface [24], such works are now being extended to multi-component cases which should speed up the computation.

Let us also mention that although the gradient flow given in (16) leads to dynamic evolution of vesicle shapes and phase changes, it should be interpreted as intermediate stages of energy minimization. More physically relevant dynamic processes can be studied such as those involving the hydrodynamic interactions of vesicles with a background fluid [5]. In our earlier works [15,18], a phase field framework has been developed to describe such dynamic processes for single-component vesicles, which can be naturally extended to the multi-component vesicle cases studied here.

Problem set up and initial profiles   We now discuss how we choose various parameters in the simulations. Though in theory the gradient flow can be started from any pair of initial phase field functions, a proper choice often speeds up the time evolution and allows more efficient solution of the equilibrium state. We note that with the penalty formulation, any of the constraints can be simply removed by setting the corresponding penalty constant zero. For example, setting $M_2 = M_3 = 0$ would eliminate the total area and area difference constraints. This fact can be utilized to find good initial phase field functions.

As an illustration, for a given $r > 0$, we may start from two special phase field functions as $\phi(\mathbf{x}) = \tanh(\frac{|\mathbf{x}| - r}{\sqrt{2}\epsilon})$ and $\eta(\mathbf{x}) = \tanh(\frac{z}{\sqrt{2}\epsilon})$ where z is the third component of $\mathbf{x}$. As depicted in Fig. 1, this provides two hemispheres that represent the two components (colored in *red* and *blue*, respectively, or in gray-scale represented by lighter and darker regions). Starting from this initial state, and setting $M_1 = 0$ to eliminate the volume constraint, the sphere gradually becomes more prolate due to the
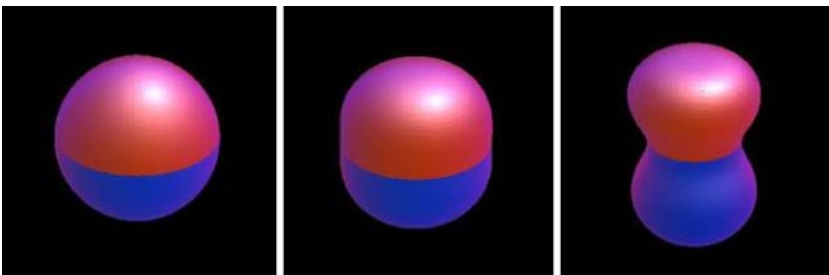

Fig. 1 Line tension drives a two-component sphere to a gourd shape

presence of line tension, then further transforms to a gourd shape. We may stop at an intermediate shape and add back the volume constraint. This would provide a variety of initial shapes to be used in the simulations.

Convergence verification   For a particular numerical simulation, the quality of the numerical result may be affected by the choice of computational domain, the parameter ϵ (the effective width of the diffuse interface), the number of grid points, and the choices of other parameters used in the simulation. The parameter ϵ is generally taken to be a few percentage points of the domain size to ensure a relatively sharp interfacial region and the consistency with the sharp interface description (the $\epsilon \to 0$ limit). The mesh size is normally taken to be several times smaller than the width of the transition layer to ensure adequate spatial resolution. To ascertain the accuracy and robustness of our numerical algorithms and the parameter selections, we here present results of some numerical tests on the convergence and performance of our method.

The first set of experiments given in Fig. 2 is designed to test the dependence of the resolution of the phase field function on the the parameter ϵ and the grid size. We take a shape similar to the previous experiment. First, we take a 64^3 spatial grid but use different values of ϵ at $0.1964(= 2h)$ and $0.1472(= 1.5h)$. The other parameters are defined by $v_d = -216.52$, $a_0 = 29.46$, $a_d = 0.23$ and $M_i = 3.2 \times 10^5$ for all i. The two equilibrium shapes are almost the same except the transition layer width. The corresponding final energy values 124.49 and 123.82 are very close to each other. The left picture of Fig. 2 gives the final 3D views and some cross-section views of the phase field functions ϕ and η.

Now we use the same set of parameters ($\epsilon = 0.1964$, same initial ϕ_0 in the same domain), but solve the problem on two different grid sizes 48^3 and 64^3. The other parameters are set to be $v_d = -216.52$, $a_0 = 29.46$, $a_d = 0.23$ and constants $M_i = 10^4$ for all i. The right picture of Fig. 2 provides the details of the simulations, with the 3D views of ϕ, and their density plots of the cross-sections in $x–z$ plane, and partial 3D views of η. The final values of energy on two different grids are 124.39 and 124.42 while the elastic bending energy values are at 48.05 and 47.96, and the line
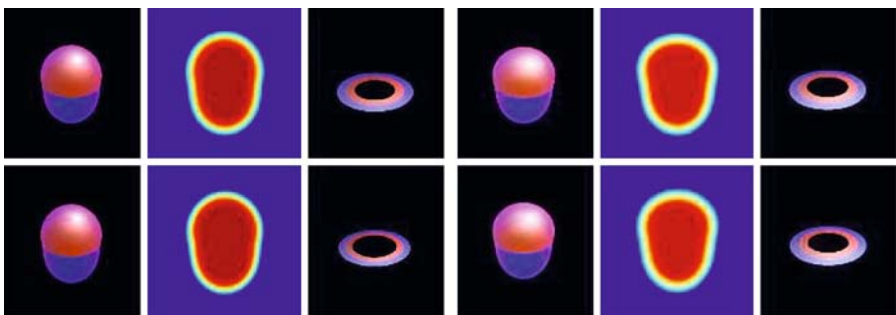

Fig. 2 The 3D and cross-section views of ϕ and the 3D view for part of η, computed with different parameters: *left picture*, $\epsilon = 2h$ (*above*) and $\epsilon = 1.5h$ (*below*); *right picture*, 64^3 grid (*above*) and 48^3 grid (*below*)

Table 1 Convergence of the Lagrange multipliers

$M_1 = M_2 = M_3$	4,000	8,000	16,000	32,000
Λ_1	−3.0781	−3.0823	−3.0946	−3.0943
$V(\phi) - v_d$ $(\times 10^{-4})$	−7.6952	−3.8528	−1.9341	−0.9669
Λ_2	3.6342	3.6430	3.6608	3.6626
$A(\phi) - a_0$ $(\times 10^{-4})$	9.0855	4.5537	2.2880	1.1445
Λ_3	0.8144	0.8144	0.8181	0.8173
$D(\phi, \eta) - a_d$ $(\times 10^{-4})$	2.0360	1.0180	0.5113	0.2554

Table 2 The diminishing effect of regularization on the total energy

$M_4 = M_5$ $(\times 10^3)$	32	16	8	4
E_4	0.1223	0.1108	0.0966	0.0798
$E_4/\mathcal{E}_M$	0.0983%	0.0892%	0.0778%	0.0643%
E_5	0.0380	0.0336	0.0285	0.0227
$E_5/\mathcal{E}_M$	0.0305%	0.0270%	0.0229%	0.0182%
$\mathcal{E}_M$	124.2942	124.2027	124.1209	124.0500

tension energy values at 76.34 and 76.46, respectively. The close values substantiate the numerical convergence of the simulated results.

The convergence can also be verified for different penalty and regularization constants $\{M_i\}_{i=1}^5$. The difference in adopting the penalty and/or the regularization is to be understood as follows: the penalty constants $\{M_i\}_{i=1}^3$ are taken to be larger and larger to ascertain the satisfaction of the volume and areas constraints. The regularization constants $\{M_4, M_5\}$, on the other hand, are taken to be smaller and smaller so that the orthogonality of the zero level sets of the two phase field functions and the tanh like profile of η are both effectively maintained in the simulations, and the associated energy contribution from the regularization terms diminishes progressively.

First, we define the Lagrange multipliers $\{\lambda_i\}_{i=1}^3$ as the limits of $\{\Lambda_i\}_{i=1}^3$ as M_1, M_2, and M_3 go to infinity, where $\Lambda_1 = M_1(V(\phi) - v_d)$, $\Lambda_2 = M_2(A(\phi) - a_0)$, $\Lambda_3 = M_3(D(\phi, \eta) - a_d)$. With other parameters given by $M_4 = M_5 = 10,000$, $v_d = -216.52$, $a_0 = 29.46$, $a_d = 0.230$, $\epsilon = 0.1736$, $h = 0.0982$, we set larger and larger values for $M_1 = M_2 = M_3$. The results are shown in Table 1 which demonstrate that Λ_1, Λ_2 and Λ_3 converge to the Lagrange multipliers, and errors in constraints also decrease.

Next, we demonstrate that the regularization terms provide effective control on the phase field functions but do not contribute significantly to the energy minimization. We set a sequence of decreasing values for M_4, M_5 while taking the same values for $M_1 = M_2 = M_3 = 10,000$, and keeping the values of other parameters the same as in the previous test. The results are given in Table 2 where $E_4 = \frac{1}{2}M_4(N(\phi, \eta))^2$ and $E_5 = \frac{1}{2}M_5(P(\eta))^2$ and their ratios with the total energy $\mathcal{E}_M$ are provided. We can observe the diminishing and negligible effect of the regularization terms while there is no noticeable change in the simulated membrane.
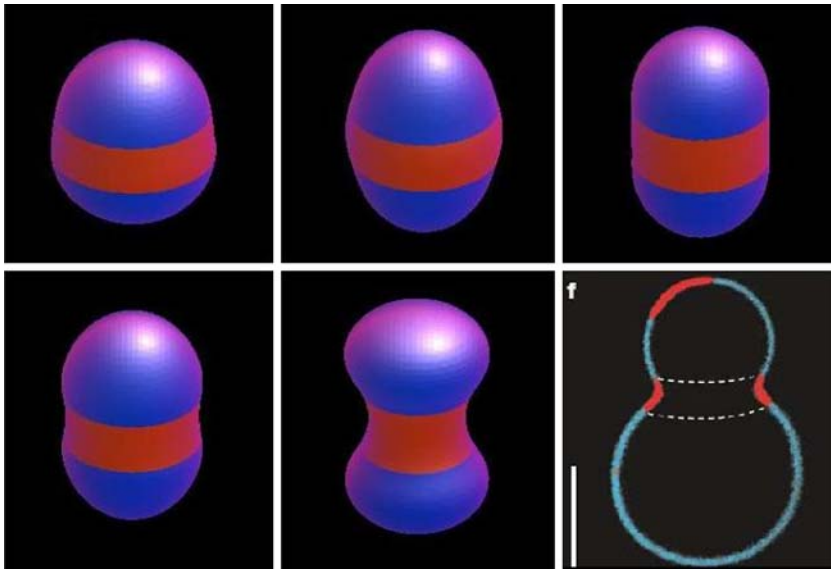
Fig. 3 Different values of bending rigidity lead to different shapes of striped vesicles (the *bottom right picture* is reproduced from [3])

Having demonstrated the convergence of the numerical algorithms, we next study the effect of different bending rigidities and various line tension constants. Then by adjusting the bending rigidities in the two components and the line tension, we can simulate the the vesicle shapes in experimental findings [3]. Unless noted otherwise, the simulation results reported in the following are obtained with $\epsilon = 0.1736$ on a 64^3 grid which can offer sufficient resolution based on the convergence study.

Effect of the bending rigidities   To examine the effect of bending rigidities on shapes of vesicles, our first experiment is a simulation of the striped vesicles. We start from an initial a stripe-looking vesicle where the red component is situated in the center with both ends being connected with the blue component in the shape of spherical caps. As shown in the first row of the Fig. 3, with parameters $v_d = -213.98$, $a_0 = 29.46$ and $a_d = -13.31$, the initial shape grows into a very regular stripe-looking ellipsoid shown in the middle of the first row. In this experiment, the bending rigidity for the red component is 1.0 whereas the blue component is 3.0. With line tension being fixed at 10.0, we then make a switch of the bending rigidity of the two components. As shown in the right picture of the first row, the red component in the middle of the ellipsoid becomes more cylindrical. Next, by preserving the bending rigidity of the blue component while increasing that of the red component from 3.0 to 19.0, the red component shrinks in diameter and we get a slender center band as shown in the left picture of the second row. It is obvious that the saddle region has a smaller mean curvature. We can further increase the area of the blue component by setting $a_0 = 33.46$ and $a_d = -19.82$, and with bending rigidities 3.8 and 0.2, respectively, for the red and blue components, we get the middle picture of the second row in Fig. 3. One can
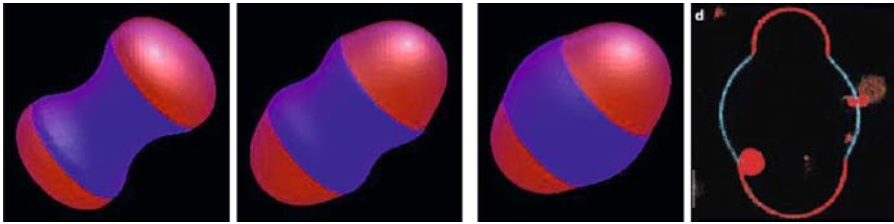
Fig. 4 Redistributing the components and changing area, volume and line tension result in different vesicle shapes

compare it with the last picture shown in the figure which corresponds to shapes found in actual experiments [3] even though the difference in the bending rigidities is not as significant as those used here.

The numerical simulation shows that the component with a larger bending rigidity remains in regions with smaller values of mean curvature in order to minimize the total bending energy, yet, it is interesting to observe that there are other shapes reported in the physical experiments showing domains of smaller bending rigidity in the center strip. For comparison purposes, we start from the last shape computed in the above and switch the portions of the two components (thus the colors), and redistribute them so that it gives an initial shape (left most of Fig. 4) with $v_d = -213.98$, $a_0 = 33.46$, $a_d = -2.54$, the line tension being 4.0 and the bending rigidities being 3.8 and 0.2, respectively, as in the last experiment, then the minimization of energy leads to a new shape (second from left in Fig. 4), demonstrating that the center strip can be occupied by either phases depending on the parameter values. Moreover, if the volume is further increased so that $v_d = -210.05$, and the line tension is increased dramatically to 40 while values for the other parameters remain unchanged, the minimizing shape becomes quite different (second from right in Fig. 4), which is similar to a shape (right most of Fig. 4) reported in the experiments of [3]. Results of this series of experiments indicate that the line tension and other parameters also play important roles, in addition to that played by the different bending rigidities. Such effects are further examined in the simulations described next.

Effect of the line tension constant   By intuition, we expect that larger line tension generally leads to a shorter phase boundary between two different components. And the line tension is balanced by the bending and elasticity force, the volume and surface area constraints. In most of the cases, the volume constraint plays a key role in balancing a large line tension as in the experiments illustrated in Figs. 5 and 6.

In Fig. 5, the pictures shown there correspond to equilibrium shapes with three different values of the line tension 10.0, 30.0, 100.0. The bending rigidities of the blue colored component is 3.5 while that of the red is 0.5. By increasing the line tension, the individual components in the two-component vesicle become more like spherical caps which are resulted from the stronger effect of the line tension under the same volume and surface area constraints.

Figure 6 gives an even more convincing example to the rupture and vesicle fission observed in this process. As shown in Fig. 6, we start from the top left shape. While
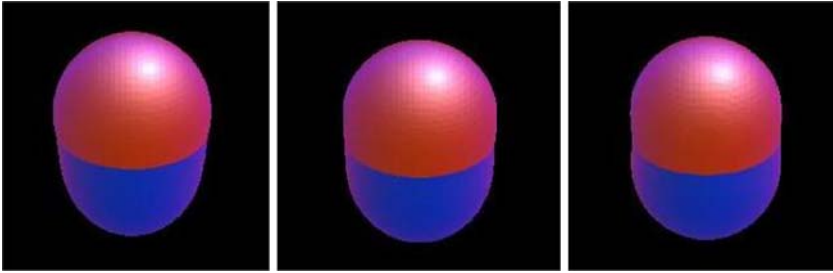
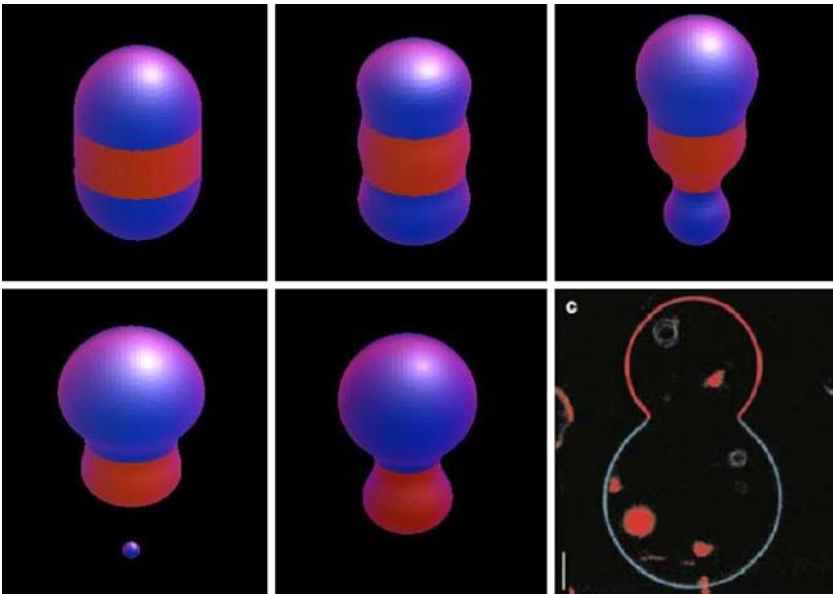**Fig. 5** Different values of line tension result in different vesicle shapes

Fig. 6 Effect of line tension: rupture and fission of vesicles components (the *right bottom picture* is reproduced from [3])

preserving v_d, a_0 and a_d to be -213.98, 29.46 and -13.31, respectively, we increase significantly the line tension from 10.0 to 100.0. The vesicle gradually breaks its vertical symmetry and a small blue vesicle is separated and eventually absorbed into the top portion through a process like Oswald ripening. Finally, the vesicle (bottom-right picture of Fig. 6) only contains two parts, much like the shape observed in the experiments [3].

Comparison with other experimental results   We now focus on the simulations that mimic other two-component vesicle shapes observed in the experiments of [3], similar to the results depicted in Figs. 3 and 6.

   As shown in the two rows of Fig. 7, we carry out two simulations starting from a shape given on the left. In both simulations, the red component has bending rigidity
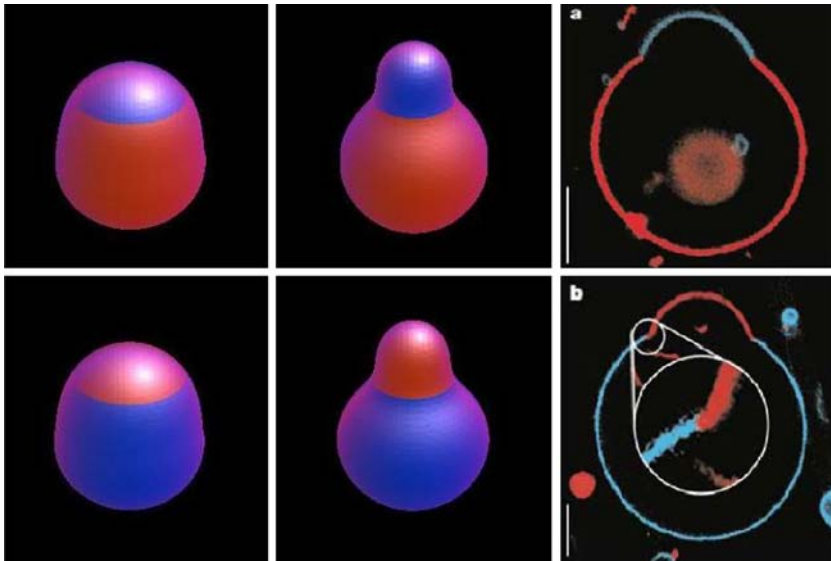
Fig. 7 Similar membrane shapes with different areas for the two components (the pictures on the *right column* are reproduced from [3])

Table 3 Energy comparison for the shapes given in Fig. 7

Energy	E_r	E_b	$E_r + E_b$	E_l	$E_r + E_b + E_l$
Top	58.36	12.15	70.51	138.17	208.68
Bottom	34.83	20.06	54.89	138.01	192.90

3.0, and the blue component has bending rigidity 1.0. The line tension between two components is 30.0. We also use $v_d = -218.0$, $a_0 = 29.46$ while take a_d as 18.76 and -18.76, respectively. The final shapes of the two simulations are shown in the center pictures of both rows. One can compare them with the right most experimental picture provided in [3].

The energy values of the two experiments illustrated in Fig. 7 are given in Table 3 with energy contributions listed for individual components and the line tension from the phase boundary. We get almost the same line tension energy contribution, but, as caused by the difference in the bending rigidities, the elastic bending energy contributions differ by a factor of 3, which is reflective of the ratio of the bending rigidities.

We now turn to simulate a couple of other interesting shapes experimentally observed in [3] as illustrated in the last pictures of Figs. 8 and 11, respectively. In Fig. 8, we first start from a spherical surface which is divided into two components where one component occupies similar spherical caps in twelve well-spaced locations on the membrane surface. The bending rigidity is 3.5 for the red component and 0.5 for the blue component, and the line tension is 10.0. With a larger surface area of the blue component and a smaller volume than those values for the exact sphere, the blue component (with smaller bending rigidity) starts to bulge (the second picture). The parameters are taken respectively as $v_d = -174.17$, $a_0 = 54.63$ and $a_d = 11.01$. If
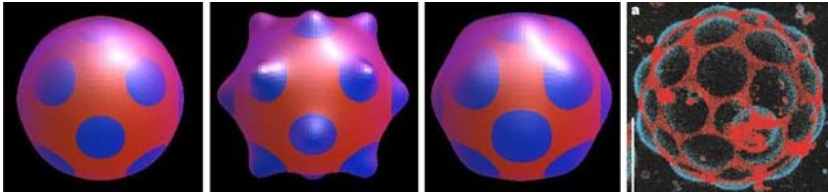
Fig. 8 A sphere with disk like bumps: comparing with biological experiments
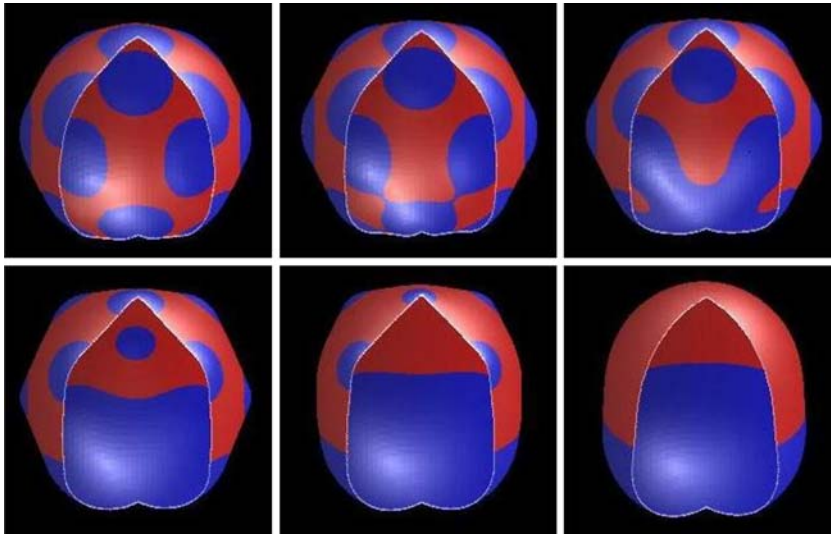

Fig. 9 The coarsening and merging of blue component (cut view)

we further increase the volume and enlarge the relative area of the blue component ($v_d = -167.0$, $a_0 = 54.63$ and $a_d = 5.0$), the resulting computed shape (the third picture in Fig. 8) becomes very similar to the experiment findings [3] (the last picture in Fig. 8).

The shape corresponding to the third picture of Fig. 8 stays as a near equilibrium (meta-stable) state for a range of parameter values. But if we continue to increase the area of the blue component, for example, by setting $a_d = 2.5$, additional coarsening of the blue component then starts to take place. The merger of disconnected components continues, much like the Oswald ripening effect, and the vesicle eventually transforms into shapes similar to that presented earlier in Figs. 2 and 5. The transformation is illustrated in Fig. 9.

Next, we take an initial membrane profile similar to that in the second picture of Fig. 8. By setting $v_d = -203.0$, $a_0 = 54.63$ and $a_d = 5.0$ so that both the total volume and the area of the red components are decreased, we can then observe the budding growth of bumps of the red component, leading to a shape shown in the right pictures of Fig. 10. With different initial profiles, other equilibrium shapes as shown in the left and center pictures in Fig. 10 have also been observed in our simulations.
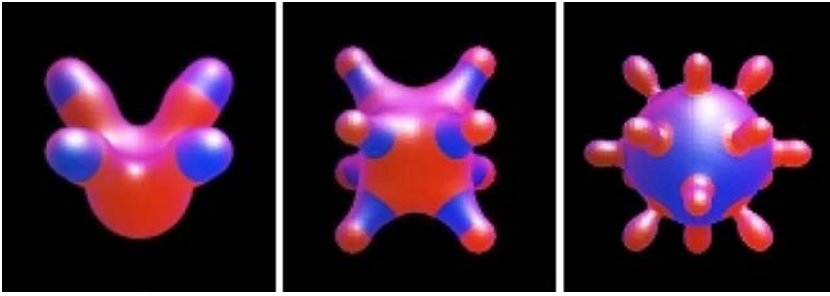
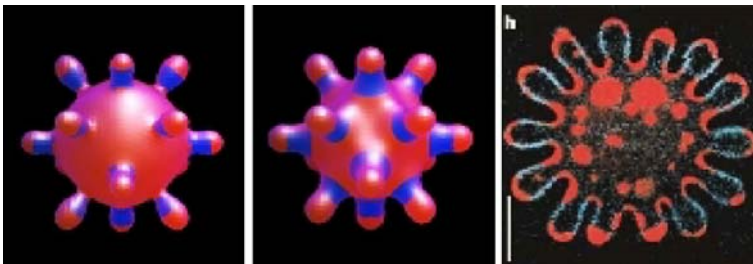**Fig. 10** Various shapes of two-component membranes

Fig. 11 Two-component shape with 14 bumps (the last picture is from [3])

From Fig. 10, it can be seen that the two-component vesicles may display very rich patterns, even in the absence of spontaneous curvature effect. One naturally may wonder if some of them are experimentally observable. The next set of experiments draws inspiration from the center and right figures of Fig. 10 and leads to interesting comparisons with similar experimental observations in [3]. We start with the same phase field ϕ as the profile in the right picture of Fig. 10, but use a modified η such that the neck of the bumps are formed by the blue component as the case of the center picture of Fig. 10. This leads to an initial shape as shown in the left picture of Fig. 11. Setting the parameters as $v_d = -203.0$, $a_0 = 54.63$, and $a_d = 22.68$, we finally get a shape (center picture of Fig. 11) very close to the experimentally observed shape given in [3] (right picture of Fig. 11).

Shapes depicted in Fig. 11 are fairly robust. In fact, with a slight modification of the final shape and a rotation in a given angle, we find that the gradient flow again leads to an equilibrium solution in the shape (except for a rotation). Results of such calculations on both 64^3 and 96^3 grids are given in Fig. 12 for comparison.

Before ending the discussion on numerical simulations of two-component vesicles, let us mention that while much of the results are only qualitatively compared with the experiments given in [3], due to the incomplete account of all the energy contributing factors (e.g., there is no consideration on the Gaussian curvature and spontaneous curvature effects), some quantitative comparisons are also feasible, in fact, the parameters corresponding to the physical experiments can be recovered from the numerical values assigned in the current work via the following scaling: bending rigidity corresponds to $k \times 1.9 \times 2 \times 10^{-19}$ J, line tension $\delta \times 0.89 \times 10^{-13}$ N, and the box size $2\pi \times 2 \times 10^{-6}$ m.
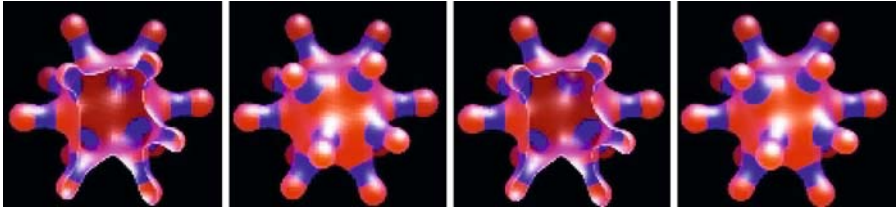
Fig. 12 Rotated two-component shapes with 14 bumps computed by different meshes

So as an example, the simulation depicted in Fig. 11 would roughly correspond to having the following parameters in the physical experiments of [3]: the bending rigidity for the blue phase is 1.3×10^{-18} J and for the red phase is 1.9×10^{-19} J, the line tension is 8.9×10^{-13} N, while the side length of the box is 12.6 µm. These values fit very well the range of estimated experimental parameters [3].

4 Open liposomal membranes

In this section, we apply similar ideas to model open lipid membranes. The transformations from vesicles to open membranes and the reverse process from open membranes to vesicles were first observed in [36]. Here, we only consider the one-component open membranes with specified surface areas. The total energy of an open membrane Γ with edge γ_0 may be conveniently defined as the sum of the elastic bending energy and the line tension energy [9,40–42,44]:

$$\int_{\Gamma} \left(a_1 + a_2(H - c_0)^2 + a_3 G \right) ds + \int_{\gamma_0} \delta \, dl.$$

For simplicity, we set the surface tension a_1 and the line tension δ, as two constants, we do not consider the contribution of the geodesic curvature term in the line energy on the boundary (thus ignoring the Gaussian rigidity, see again the Appendix B), nor the effects of spontaneous curvatures. Our problem is then to minimize the following total energy

$$E_o = \int_{\Gamma} k H^2 \, ds + \int_{\gamma_0} \delta \, dl$$

with prescribed surface area $|\Gamma|$.

Most of the available numerical simulations for open membranes have largely been confined to axis-symmetric cases based on the variational calculation of the above energy. We hereby develop a new phase field model for open membranes, and present some numerical simulations for the full 3D case to demonstrate the effectiveness of the model.
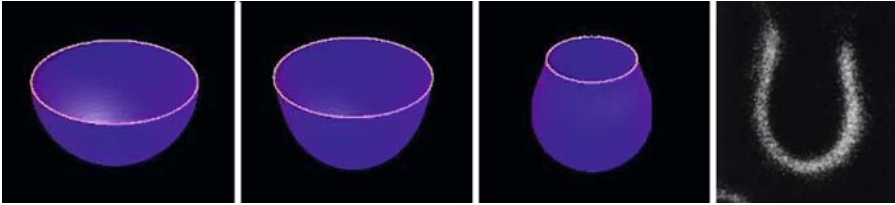
Fig. 13 Open membranes with different line tensions (the *right most picture* is reproduced from [36])

Phase field model for open membranes We can treat open membranes as two-component membranes with one component having zero bending rigidity. Again, we let γ_0 be the intersection of two orthogonal surfaces Γ and $\Gamma_\perp$ which are implicitly defined as the level-set of the functions ϕ and η, respectively.

Now we denote $c(\eta) = \frac{1}{2}(1 + \tanh(\frac{\eta}{\xi}))$, and let the line tension energy be still formulated by $L(\phi, \eta)$ in (4), with the elastic bending energy of the membrane

$$E(\phi, \eta) = \int_\Omega \frac{kc(\eta)}{2\epsilon} \left(\epsilon \Delta\phi + \frac{1}{\epsilon}\phi(1 - \phi^2) \right)^2 dx.$$

Then, our phase field model for open membranes is to minimize $E(\phi, \eta) + L(\phi, \eta)$ with the surface area constraint

$$D(\phi, \eta) = \int_\Omega c(\eta) \left[\frac{\epsilon}{2}|\nabla\phi|^2 + \frac{1}{4\epsilon}(\phi^2 - 1)^2 \right] dx = a_0. \qquad (17)$$

Similar to the two-component vesicle case studied earlier, to maintain the good profiles for both phase field functions ϕ and η and the orthogonality of Γ and $\Gamma_\perp$, we can again take the penalty formulation

$$\mathcal{E}_M(\phi, \eta) = W(\phi, \eta) + L(\phi, \eta) + \frac{1}{2}M_3(D(\phi, \eta) - a_0)^2$$
$$+ \frac{1}{2}M_4(N(\phi, \eta))^2 + \frac{1}{2}M_5(P(\eta))^2 + \frac{1}{2}M_6(P(\phi))^2, \qquad (18)$$

and use a gradient flow like (16) to compute the equilibrium shapes by a similar numerical scheme as that given in Sect. 3.

Numerical simulations of open membranes We now present some numerical simulations of open membranes and compare them with biological experimental findings. Most of the model and simulation parameters are chosen to be in the same range as that for the two-component vesicle simulations in the earlier section.

Figure 13 gives the simulation results of a simple open membrane. Starting from a half sphere (the left picture), with bending rigidity $k = 1.0$ and line tension $\delta = 1.0$, we get an equilibrium shape shown in the second picture. If a larger line tension $\delta = 1.28$ is used, an equilibrium shape is reached as shown in the third picture. One can compare
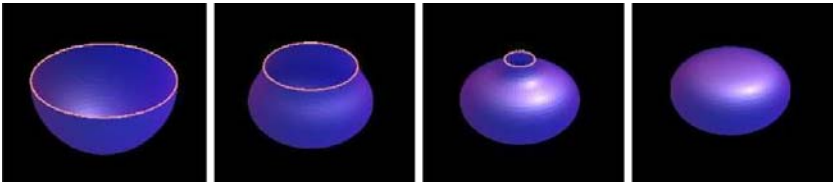
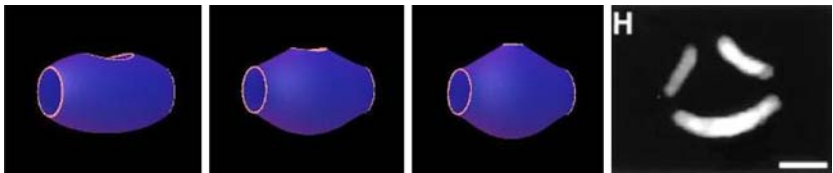**Fig. 14** Open membrane closes due to large line tension

Fig. 15 Open membranes with three holes (the *right most picture* is reproduced from [36])

it with the picture on the right which are based on experiments described in [36]. We note that the elastic bending energy are 10.12 and 15.96 and the line tension energy are 10.94 and 7.95, respectively, for the solutions in the second and third pictures.

The time evolution snapshots are given in Fig. 14 where the line tension is taken as $\delta = 25.0$. The simulation results show that, when the line tension becomes large enough, the open membrane becomes self-enclosed.

Finally, in Fig. 15, we simulate a shape (the right picture) with three holes as observed in an experiment of [36]. Starting from the left most picture corresponding to an ellipsoid with three holes, setting the bending rigidity $k = 1.0$ and line tension $\delta = 1.0$, and following the gradient flow of the energy, the initial shape starts to deform first into an intermediate shape given in the second picture. The computed equilibrium shape is shown in the third picture which again shows striking similarity with the experimental findings.

5 Conclusion

In this paper, a phase field model is formulated for the multi-component vesicles membranes, and as a special case, the open membranes with free edges. The model incorporates the effect of the elastic bending energy together with the line tension between the different components. Full 3D numerical simulations presented here demonstrate that the experimental observations given in [3] can be effectively simulated by the phase field bending elasticity and line tension model. Furthermore, the simulation results illustrate that many experimentally observed exotic patterns such as bud formation and vesicle fission can appear in two-component vesicles due to the inhomogeneous bending stiffness and the competition of the bending energy and the interfacial line tension even in the absence of the spontaneous curvature or the asymmetry of the bilayer.

In conclusion, the generalization of diffuse interface model to two-component vesicle membranes fits nicely into the previously established unified framework for

the derivation of dynamic and static equations and the development of numerical algorithms and codes, but there are many issues which remain to be examined further. For example, one may consider effective ways to formulate a more general line tension energy, incorporating the contribution of the geodesic curvature along the phase boundary, which is important to model the difference of the Gaussian rigidity in two components [2]. Similarly, in our numerical simulations, we have not examined the effect of the spontaneous curvature for two-component vesicles, unlike our study for the single component case [17]. It is expected that more complex shapes would be be discovered when these additional features are accounted for. Furthermore, the asymptotic analysis of our model, the sharp interface limit, including the effect of penalty and regularization, may be studied more rigorously, the interaction of multi-component vesicles with the fluid, protein molecules, and electric fields are also exciting topics to be investigated in the future.

Appendix A: Justification of the energy and constraints

We now provide some brief calculations to rationalize the definitions of the energy functional and the constraints in the phase field setting. Same as the discussion in [20], we first illustrate that in a general ansatz, for small ϵ and ξ, minimizing $W(\phi, \eta)$ leads to a phase field function $\phi(x)$ which is approaching to $\tanh(d(x, \Gamma)/(\sqrt{2}\epsilon))$ as $\epsilon \to 0$. In fact for small ϵ, due to the uniform bound of the functional B, the region away from the level set $\phi = 0$ are all close to $\phi = +1$ or -1. In such cases, one may define the following transformation near the interface:

$$\phi(x) = q^\epsilon \left(\frac{d(x)}{\epsilon} \right), \tag{19}$$

where $d(x)$ is the distance of the point $x \in \Omega$ to the surface Γ. Substituting this into (3), we have that

$$E(\phi) = \int_\Omega \frac{k(\eta)}{2\epsilon} \left| q^{\epsilon\prime} \left(\frac{d(x)}{\epsilon} \right) \Delta d(x) + \frac{1}{\epsilon} \left(q^{\epsilon\prime\prime} - (q^{\epsilon 2} - 1)q^\epsilon \right) \right|^2 dx. \tag{20}$$

If we keep $k(\eta)$ positive, as $\epsilon \to 0$, to minimize the energy, the leading term in the above has to vanish, that is,

$$\left| q^{\epsilon\prime\prime} - (q^{\epsilon 2} - 1)q^\epsilon \right|^2 \to 0 \tag{21}$$

which means that, with the help of far field boundary conditions, the transition region profile $q^\epsilon(\cdot)$ is approaching to the function $\tanh(\frac{\cdot}{\sqrt{2}})$. In the meantime, we see that ϕ

is approaching to the Heaviside function with values 1 inside of the interface and -1 outside. The surface Γ coincides with the zero level set of ϕ. Moreover, (19) indicates that the parameter ϵ is effectively the thickness of the transition region between $\{\phi = 1\}$ and $\{\phi = -1\}$, a fact that can be more rigorously justified [16].

Now, we take $s(\phi) = \frac{\epsilon}{2}|\nabla\phi|^2 + \frac{1}{4\epsilon}(\phi^2 - 1)^2$. When the line tension $L(\phi, \eta)$ reaches its minimum, we have

$$\frac{\delta L}{\delta \eta} = f(\eta, s) = -\epsilon \nabla \cdot (s\nabla\eta) + \frac{1}{\epsilon}s(\eta^2 - 1)\eta = 0.$$

For $\phi = \tanh(d/(\sqrt{2}\epsilon))$, we have $s = \frac{1}{2\epsilon}(\phi^2 - 1)^2$, thus $\nabla s \cdot \nabla \eta = 0$ as $\nabla\phi \cdot \nabla\eta = 0$. Then $f(\eta, s) = 0$ implies

$$-\epsilon \Delta\eta + \frac{1}{\epsilon}(\eta^2 - 1)\eta = 0.$$

If we write η again as $q^\epsilon(d(x, \Gamma_\perp)/\epsilon)$, from the above equation we have

$$-q^{\epsilon'}\left(\frac{d}{\epsilon}\right)\Delta d(x) + \frac{1}{\epsilon}\left((q^{\epsilon 2} - 1)q^\epsilon - q^{\epsilon''}\right) = 0.$$

As $\epsilon \to 0$, we have $(q^{\epsilon 2} - 1)q^\epsilon - q^{\epsilon''} = 0$. To minimize L, we expect that far away from the $\Gamma_\perp$, q^ϵ is ± 1, therefore we also have $q^\epsilon(x) = \tanh(\frac{x}{\sqrt{2}\epsilon})$. On the other hand, we can use the same argument for ϕ if we know η is a tanh function, which would further substantiate the ansatz that ϕ and η are both tanh functions to lead order of ϵ. In fact, following more careful analysis as those in [16], we expect that the differences between ϕ and η and the respective tanh profiles are second order in ϵ which would allow us to rigorously derive the asymptotic limits (8–10).

Appendix B: Gaussian curvature energy

The phase field framework developed here can be extended to include more contributing factors to the energy such as the Gaussian curvature energy. For the phase field treatment of the Gaussian curvature energy for single component vesicles, we refer to our recent work [21]. For a two-component vesicle with different Gaussian rigidities κ_G^1 and κ_G^2, using the Gauss–Bonnet theorem, the Gaussian curvature energy can be simplified to [10]

$$\sum_{j=1}^{2}\int_{\Gamma_i}\kappa_G^j G\, ds = -\left(\kappa_G^1 - \kappa_G^2\right)\int_{\gamma_0}g_s\, dl + 2\pi\sum_{j=1}^{2}\kappa_G^j\chi(\Gamma_j)$$

where $\chi(\Gamma_1)$ and $\chi(\Gamma_2)$ are the Euler numbers of $\{\Gamma_j\}_{j=1}^{2}$. For the moment, we consider only the case that the vesicle does not undergo any topological change so that

we may ignore the constant part and write the Gaussian curvature energy equivalently as

$$E_G = -\left(\kappa_G^1 - \kappa_G^2\right) \int_{\gamma_0} g_s \, dl.$$

Here dl is the line element (differential) along the the boundary of Γ_1 and Γ_2 with l denoting the arc length variable.

In our phase field model, the boundary line (curve) between components is represented by the intersection of two surfaces $\phi(x) = \eta(x) = 0$. Then, its unit tangent vector T is perpendicular to both $\nabla\phi$ and $\nabla\eta$. With a proper choice of the orientation of the line element the direction of T can be taken as $-\nabla\phi \times \nabla\eta$. Thus, with normalization, we get

$$T = -\frac{\nabla\phi}{|\nabla\phi|} \times \frac{\nabla\eta}{|\nabla\eta|}.$$

Here, the definition of T works for any curve through a point x which is parallel to γ_0. The geodesic curvature can be expressed as [10]

$$g_s = (n \times T) \cdot \frac{dT}{dl}$$

where n is the normal of the vesicle surface. In our phase field formulation, $n = \frac{\nabla\phi}{|\nabla\phi|}$ and $dT/dl = (\nabla \times T) \times T = (T \cdot \nabla)T$. Then

$$g_s = \frac{\nabla\eta}{|\nabla\eta|} \cdot ((T \cdot \nabla)T).$$

Similar to the formula of the line tension, we have

$$\int_{\gamma_0} g_s \, dl = \left(\frac{3}{2\sqrt{2}}\right) \frac{1}{2} \int_\Omega g_s(x)\xi|\nabla\eta|^2|\nabla\phi| \, dx$$

$$= \frac{3\sqrt{2}\xi}{8} \int_\Omega \nabla\eta \cdot ((\nabla\phi \times \nabla\eta) \cdot \nabla) \frac{\nabla\phi \times \nabla\eta}{|\nabla\phi||\nabla\eta|} \, dx.$$

All together, the Gaussian curvature energy used in our phase field model may be given by

$$E_G = -\frac{3\sqrt{2}}{8}\xi(\kappa_G^1 - \kappa_G^2) \int_\Omega \nabla\eta \cdot ((\nabla\phi \times \nabla\eta) \cdot \nabla) \frac{\nabla\phi \times \nabla\eta}{|\nabla\phi||\nabla\eta|} \, dx, \qquad (22)$$

if there is no topological change in the vesicle. To provide a more general framework that remains valid even with the change of topology, we may extend the work in [21]

based on the phase field representation of the Gaussian curvature. In particular, we may represent $\sum_{j=1}^{2} \int_{\Gamma_j} k_G^j G ds$ by

$$\frac{1}{c} \int_{\Omega} k_G(\eta) G(\phi) \, dx$$

where $k_G(\eta)$ gives the respective Gaussian rigidities in the two components when $\eta = \pm 1$, c is a normalization constant and the Gaussian curvature $G(\phi)$ can be constructed in different ways depending on the properties of the phase field function ϕ. A very general form (thus requiring fewer assumptions on ϕ) is given in [21]:

$$G(\phi) = \frac{1}{|\nabla \phi|} \Lambda \left(\nabla^2 \phi - \frac{\nabla \phi \cdot \nabla^2 \phi \cdot \nabla \phi}{|\nabla \phi|^4} \nabla \phi \otimes \nabla \phi \right)$$

where $\lambda(M)$, for a 3×3 matrix M, denotes the the sum of the determinants of its three principal minors. Various simpler forms are proposed in [19], for instance,

$$G(\phi) = \frac{1}{\alpha_n \epsilon} \left(\Delta \phi + \frac{1}{\epsilon^2} \phi (1 - \phi^2) \right) p_n(\phi)$$

with $p_n(t) = 2n(1 - t^2)^{n-1} t$ and $\alpha_n = 2 \int_{-\infty}^{\infty} (\tanh(s/\sqrt{2})^2 - 1)^n \, ds$ for some integer $n \geq 1$. Such simplifications are valid for ϕ in a special ansatz such as the particular form of $\phi(x) = \tanh(d(x, \Gamma)/\sqrt{2}\epsilon)$ where $d(x, \Gamma)$ is the signed distance function to the zero level set surface Γ [20].

The above discussion provides possible approaches to incorporate the Gaussian curvature contributions for two-component vesicles. Their numerical implementation, analytical and experimental validations will be carried out in future works.

References

1. Anderson, D., McFadden, G., Wheeler, A.: Diffuse-interface methods in fluid mechanisms. Annu. Rev. Fluid Mech. **30**, 139–165 (1998)
2. Baumgart, T., Das, S., Webb, W., Jenkins, J.: Membrane elasticity in giant vesicles with fluid phase coexistence. Biophys. J. **89**, 1067–1080 (2005)
3. Baumgart, T., Hess, S., Webb, W.: Imaging coexisting fluid domains in biomembrane models coupling curvature and line tension. Nature **425**, 821–824 (2003)
4. Benvegnu, D., McConnell, M.: Line tension between liquid domains in lipid monolayers. J. Phys. Chem. **96**, 6820–6824 (1992)
5. Biben, T., Kassner, K., Misbah, C.: Phase-field approach to 3D vesicle dynamics. Phys. Rev. E **72**, 041921 (2005)
6. Boettinger, W., Warren, J., Beckermann, C., Karma, A.: Phase-field simulation of solidification. Ann. Rev. Mater. Res. **32**, 163–194 (2002)
7. Burchard, P., Cheng, L.-T., Merriman, B., Osher, S.: Motion of curves in three spatial dimensions using a level set approach. J. Comput. Phys. **170**, 720–741 (2001)
8. Caginalp, G., Chen, X.F.: Phase field equations in the singular limit of sharp interface problems. In: On the Evolution of Phase Boundaries (Minneapolis, MN, 1990–1991), pp. 1–27. Springer, New York (1992)
9. Capovilla, R., Guven, J., Santiago, J.: Lipid membranes with an edge. Phys. Rev. E **66**, 021607 (2002)

10. Carmo, M.: Differential Geometry of Curves and Surfaces. Prentice-Hall, Englewood Cliffs (2006)
11. Chen, L.-Q.: Phase-field models for microstructure evolution. Annu. Rev. Mater. Res. **32**, 113–140 (2002)
12. Ciarlet, P.G.: Introduction to Linear Shell Theory. Gauthier-Villars and Elsevier, Paris (1998)
13. Ciarlet, P.G.: Mathematical elasticity, III: Theory of shells. In: Studies in Mathematics and its Applications. North-Holland, Amsterdam (2000)
14. Döbereiner, H., Käs, J., Noppl, D., Sprenger, I., Sackmann, E.: Budding and fission of vesicles. Biophys. J. **65**, 1396C1403 (1993)
15. Du, Q., Li, M., Liu, C.: Analysis of a phase field Navier–Stokes vesicle-fluid interaction model. Disc. Cont. Dyn. Sys. B. **8**(3), 539–556 (2007)
16. Du, Q., Liu, C., Ryham, R., Wang, X.: A phase field formulation of the Willmore problem. Nonlinearity **18**, 1249–1267 (2005)
17. Du, Q., Liu, C., Ryham, R., Wang, X.: Modeling the spontaneous curvature effects in static cell membrane deformations by a phase field formulation. Commun. Pure Appl. Anal. **4**, 537–548 (2006)
18. Du, Q., Liu, C., Ryham, R., Wang, X.: Modeling vesicle deformations in flow fields via energetic variational approaches (2006, preprint)
19. Du, Q., Liu, C., Ryham, R., Wang, X.: Diffuse interface energies capturing the euler number: relaxation and renormalization. Commun. Math. Sci. **5**, 233–242 (2007)
20. Du, Q., Liu, C., Wang, X.: A phase field approach in the numerical study of the elastic bending energy for vesicle membranes. J. Comput. Phys. **198**, 450–468 (2004)
21. Du, Q., Liu, C., Wang, X.: Retrieving topological information for phase field models. SIAM J. Appl. Math. **65**, 1913–1932 (2005)
22. Du, Q., Liu, C., Wang, X.: Simulating the deformation of vesicle membranes under elastic bending energy in three dimensions. J. Comput. Phys. **212**, 757–777 (2006)
23. Du, Q., Wang, X.: Convergence of numerical approximations to a phase field bending elasticity model of membrane deformations. Inter. J. Numer. Anal Model. **4**, 441–459 (2007)
24. Du, Q., Zhang, J.: Adaptive finite element method for a phase field bending elasticity model of vesicle membrane deformations (2007, preprint)
25. Gozdz, W., Gompper, G.: Shapes and shape transformations of two-component membranes of complex topology. Phys. Rev. E **59**, 4305–4316 (1999)
26. Jiang, Y., Lookman, T., Saxena, A.: Phase separation and shape deformation of two-phase membranes. Phys. Rev. E **6**, R57–R60 (2000)
27. Juelicher, F., Lipowsky, R.: Shape transformations of vesicles with intramembrane domains. Phys. Rev. E **53**, 2670–2683 (1996)
28. Kumar, P., Gompper, G., Lipowsky, R.: Phys. Rev. Lett. **86**, 3911–3914 (2001)
29. Lipowsky, R.: Budding of membranes induced by intramembrane domains. Journal de Physique II, France **2**, 1825–1840 (1992)
30. Lipowsky, R.: The morphology of lipid membranes. Curr. Opin. Struct. Biol. **5**, 531–540 (1995)
31. Lipowsky, R.: Domains and rafts in membranes hidden dimensions of self-organization. J. Biol. Phys. **28**, 195–210 (2002)
32. McWhirter, J., Ayton, G., Voth, G.: Coupling field theory with mesoscopic dynamical simulations of multicomponent lipid bilayers. Biophys. J. **87**, 3242–3263 (2004)
33. Mukherjee, S., Maxfield, F.: Membrane domains. Annu. Rev. Cell Dev. Biol. **20**, 839–866 (2004)
34. Ou-Yang, Z., Liu, J., Xie, Y.: Geometric Methods in the Elastic Theory of Membranes in Liquid Crystal Phases. World Scientific, Singapore (1999)
35. Osher, S., Fedkiw, R.: The Level Set Method and Dynamic Implicit Surfaces. Springer, Heidelberg (2002)
36. Saitoh, A., Takiguchi, K., Tanaka, Y., Hotani, H.: Opening-up of liposomal membranes by talin. Proc. Natl. Acad. Sci. Biophys. **956**, 1026–1031 (1998)
37. Seifert, U.: Curvature-induced lateral phase separation in two-component vesicles. Phys. Rev. Lett. **70**, 1335–1338 (1993)
38. Sethian, J.A.: Level Set Methods and Fast Marching Methods: Evolving Interfaces in Computational Geometry, Fluid Mechanics, Computer Vision, and Materials Science. Cambridge University Press, New York (1999)
39. Simons, K., Vaz, W.: Model systems, lipid rafts, and cell membranes. Annu. Rev. Biophys. Biomol. Struct. **33**, 269–295 (2004)
40. Tu, Z., Ou-Yang, Z.: Lipid membranes with free edges. Phys. Rev. E **68**, 061915 (1–7) (2003)

41. Tu, Z., Ou-Yang, Z.: A geometric theory on the elasticity of bio-membranes. J. Phys. A Math. Gen. **37**, 11407–11429 (2004)
42. Umeda, T., Suezaki, Y., Takiguchi, K., Hotani, H.: Theoretical analysis of opening-up vesicles with single and two holes. Phys. Rev. E **71**, 011913 (1–8) (2005)
43. Wang, X.: Phase Field Models and Simulations of Vesicle Bio-membranes. Ph.D thesis, Department of Mathematics, Penn State University (2005)
44. Yin, Y., Yin, J., Ni, D.: General mathematical frame for open or closed biomembranes I: Equilibrium theory and geometrically constraint equation. J. Math. Biol. **51**, 403–413 (2005)